



Physically- and Knowledge-Informed deep learning for robust prediction of martensite start temperature in steels

Pengxin Wang ^{a,b}, G.M.A.M. El-Fallah ^{a,*}

^a School of Engineering, University of Leicester, Leicester LE1 7RH, UK

^b Nanjing Iron & Steel United Co., Ltd., Nanjing, Jiangsu 210035, China



ARTICLE INFO

Keywords:

Martensite start temperature (M_s)
Phase transformation
Physics-informed machine learning
Transformer fusion model
Deep Learning

ABSTRACT

Accurate prediction of the martensite start temperature (M_s) is essential for optimising the mechanical performance of steels and enabling data-driven alloy design. This study proposes, for the first time, a physics- and knowledge-informed multi-branch Transformer fusion model that integrates chemical composition, physical features, and empirical equation-based features for precise M_s prediction. A curated dataset of 1100 steel samples was compiled from peer-reviewed studies and technical reports published between 1973 and 2023, with a primary focus on structural steels, encompassing a comprehensive range of compositional and physical variables relevant to phase transformation behaviour. The model architecture employs dedicated multilayer perceptron (MLP) branches for each feature group, followed by a Transformer encoder to capture global dependencies and nonlinear interactions. Compared with baseline models, including conventional MLPs and lasso regression, the proposed model achieves superior predictive performance (RMSE = 33.9 °C, MAE = 14 °C, $R^2 = 0.94$). SHAP-based interpretability analysis reveals that the model identifies C, Ni, and Ceq as key contributors, forming a dominant Ni–Ce–C interaction network modulated by structural descriptors. Sensitivity analyses confirm these trends and support the model's physical consistency. To experimentally validate the model, dilatometry tests on two newly designed steels confirmed that the predicted M_s values (231 °C and 165 °C) closely matched the experimental results (238 °C and 169 °C), with deviations of only 7 °C and 4 °C, respectively. This work establishes a novel, physically grounded, and interpretable machine learning framework for M_s prediction, highlighting the value of integrating physics-based knowledge with advanced deep learning to accelerate alloy design and mechanical property optimisation.

1. Introduction

The martensite start temperature (M_s) is a critical parameter in the design and heat treatment of steels, as it determines the onset of martensitic transformation from austenite during rapid cooling. Accurate prediction of M_s plays a crucial role in alloy design, heat treatment optimisation, and microstructural control of steels [1–3].

Transportation structures and vehicles, TRIP-assisted steels are widely used for their strength, ductility and energy absorption. This response relies on metastable retained austenite, whose fraction and stability are tuned across alloy systems [4,5]. Accurate prediction of martensitic transformation, especially the M_s , is critical because it defines the window in which retained austenite forms and remains stable. In quenching and partitioning steels, quenching between M_s and the martensite finish temperature M_f followed by carbon partitioning

enriches and stabilises austenite while tempering martensite, so M_s sets the target quench temperature and governs the achievable retained-austenite fraction [6]. In bainitic rail steels, heat treatment is designed around M_s to keep transformation in the bainitic regime and avoid martensite that harms rolling contact fatigue resistance [7]. Reliable estimation of transformation temperatures, particularly M_s , underpins the design and processing of transportation steels. Traditionally, the measurement of M_s relies primarily on dilatometry or metallographic analysis [8–10]. Although these methods yield reliable results, they are often time-consuming and costly. To simplify the prediction process, numerous empirical equations have been developed based on the chemical composition of steels [11–22], such as the Andrews equation [11], Kunitake equation [12], and Steven & Haynes equation [13]. These equations generally adopt a linear combination of elemental contents to calculate M_s . However, the applicability of these

* Corresponding author.

E-mail address: gmae2@leicester.ac.uk (G.M.A.M. El-Fallah).

empirical models is often limited. When the steel composition exceeds a certain range or contains multiple complex alloying elements, their prediction errors tend to increase significantly [23].

To improve the accuracy of M_s prediction, some researchers have developed thermodynamic models to estimate M_s based on the driving force of phase transformation. For example, Ghosh and Olson [24] constructed a thermodynamic model for M_s prediction considering the balance of driving force during martensitic transformation, which exhibited good physical interpretability. Nevertheless, this type of model heavily depends on thermodynamic databases and still shows limitations in high-dimensional multi-component alloy systems.

In recent years, machine learning has emerged as a central driver of alloy design and property prediction by enabling the discovery of complex structure-processing-property relations and by supporting both forward and inverse design. Lee et al. [25] developed an integrated machine-learning platform for thermo-mechanically controlled processed steels that incorporates 16 algorithms and 5473 industrial records (combining composition and processing descriptors) to predict yield strength and ultimate tensile strength; seven non-linear models achieved acceptable hold-out performance (test-set coefficient of determination $\approx 0.6\text{--}0.7$; mean squared error $< 10^{-2}$), and inverse design based on the Non-dominated Sorting Genetic Algorithm II together with high-dimensional design-space visualisation identified high-strength candidate alloys while highlighting solution diversity. Chen et al. [26] built an interpretable machine-learning pipeline for dual-phase high-ductility automotive steels (469 records) to predict ultimate tensile strength and total elongation; using physics-based descriptors (intercritical austenite fraction and austenite carbon content), a seven-feature gradient-boosting regressor achieved coefficients of determination of approximately 0.98 for ultimate tensile strength and 0.94 for total elongation (cross-validation ≈ 0.93), identified the third overageing-zone stage as dominant, generalised to another production line, and suggested an overageing-zone-three temperature window of approximately 279–288 °C for strength-ductility balance. Capdevila et al. [27] first employed artificial neural networks (ANN) for M_s prediction, demonstrating superior fitting performance compared with traditional empirical equations. Subsequently, Lu et al. [28] incorporated austenitising temperature as an auxiliary feature, which significantly improved the prediction accuracy. Wang et al. [29] proposed a convolutional neural network (CNN) model that integrated chemical compositions with multi-scale energy features, achieving high-precision prediction of M_s in complex steels. Moreover, Yan et al. [30] revealed that the prediction accuracy of ML models could be further enhanced by introducing more physical knowledge or intermediate physical features (AP features).

As summarised in previous studies, the methodologies for predicting M_s have evolved from early empirical equations to thermodynamic-based approaches and, more recently, to data-driven ML models, as

illustrated in Fig. 1. This progression reflects a technological shift from simple linear formulations to physically grounded modelling and ultimately to multivariable ML frameworks. While each paradigm has contributed to the advancement of M_s prediction, all exhibit intrinsic limitations. A key direction in current research is the incorporation of physical principles into data-driven models, which is essential for improving both interpretability and generalisation.

Despite substantial progress, several challenges continue to hinder accurate M_s prediction. Most existing ML models rely solely on chemical composition, neglecting physical mechanisms or domain knowledge. Moreover, empirical equations, representing decades of metallurgical insight, are rarely utilised in a structured manner within ML frameworks. These limitations are compounded by small datasets, high-dimensional feature spaces, and restricted generalisation performance [31,32].

In this study, motivated by the need to enhance both accuracy and interpretability in M_s prediction, we propose a novel multi-branch deep learning model that, for the first time, integrates physical descriptors and empirical equations into a machine learning framework. Three types of multi-source information are incorporated: chemical composition features, physical features (including valence electron concentration (VEC), atomic size mismatch (Δr), mixing entropy (ΔS_{mix}), and carbon equivalent (Ceq)), and empirical equations derived from metallurgical knowledge. Each feature group is processed through an independent neural network branch for targeted feature extraction, followed by feature fusion in an integrated layer to predict the M_s . Furthermore, the Optuna framework is employed to conduct automatic hyperparameter optimisation, thereby further enhancing model performance and stability. To assess feature contributions and model interpretability, SHAP analysis, feature interaction visualisation, and element-wise sensitivity analysis were performed. Furthermore, the model's practical reliability was validated by dilatometry experiments and optical microscopy characterisation on two designed steels, with predicted M_s values showing excellent agreement with experimental results. The proposed approach exhibits excellent performance in terms of prediction accuracy, feature scalability, and model interpretability, providing a new technical route for intelligent alloy design and microstructure control in steels. Accordingly, the proposed framework targets the property space relevant to transportation steels and supports alloy and process design for bridge girders, rails, and vehicle safety components.

2. Methods

In this study, a high-quality dataset comprising 1100 samples was compiled from the literature [33–46] to develop predictive models for the M_s of steels. The input features include 15 chemical composition variables (C, Mn, Si, Cr, Ni, Mo, V, Co, Al, W, Cu, Nb, Ti, B, N), four physical features (VEC, Δr , ΔS_{mix} , Ceq), and nine empirical equation

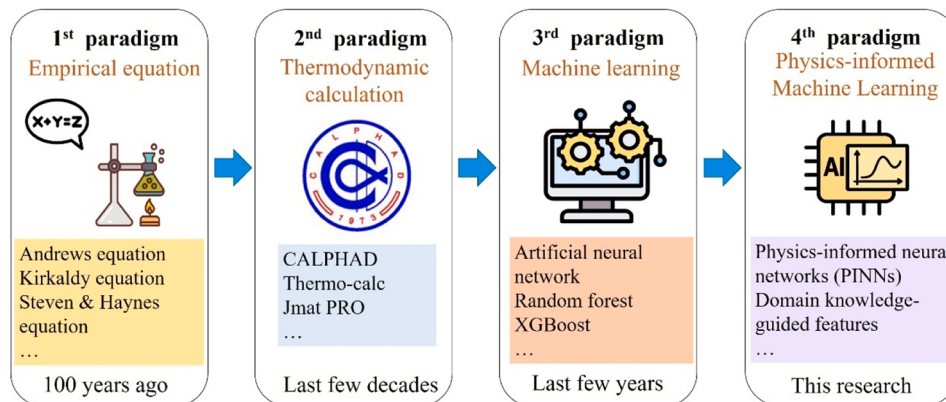


Fig. 1. Progressive development of M_s prediction methods: empirical equations, thermodynamic models, machine learning, and physics-informed machine learning.

features (M_s -Eq.1 to M_s -Eq.9), amounting to a total of 28 input variables. Detailed descriptions of the dataset and preprocessing procedures are provided in the [Supplementary Material](#) under Data Collection and Description and Data Preprocessing.

The inclusion of chemical composition features is essential for predicting M_s , as alloying elements strongly influence the relative stability of austenite (γ) and ferrite (α). Austenite-stabilising elements such as C, Mn, Ni, and Cr lower the free energy of the γ -phase, thereby suppressing the $\gamma \rightarrow \alpha$ transformation and reducing M_s . In contrast, ferrite-stabilising elements like Mo and V promote α -phase stability, increasing M_s . These effects arise from changes in the chemical driving force, shifts in phase boundaries, and modifications in transformation kinetics due to altered diffusion behaviour at the γ/α interface [47]. Therefore, chemical composition plays a pivotal role in capturing the fundamental thermodynamic and kinetic mechanisms that govern M_s .

In addition to elemental features, four physical descriptors were included in the model: VEC, Δr , ΔS_{mix} and Ceq. Although VEC, Δr , and ΔS_{mix} were initially developed in the context of high-entropy alloys (HEAs) to describe phase stability, lattice distortion, and configurational entropy [48,49], their physical principles are equally applicable to conventional steels. These features represent the multi-element interactions that influence phase transformation behaviour and mechanical performance in complex alloy systems. Ceq, by contrast, is an empirical engineering parameter widely used to estimate hardenability and weldability based on the combined effect of various alloying elements. It indirectly reflects phase transformation tendencies and is thus relevant to M_s prediction. Together, these physical features offer complementary insights beyond basic composition, bridging theoretical understanding and practical alloy design.

The four physical features are composition-derived and therefore available for all records, which ensures consistency across literature sources and avoids bias from sparsely reported processing metadata. Valence electron concentration VEC reflects band filling and phase stability and is widely used to discriminate ferrite austenite tendencies, which in turn governs transformation paths and the attainable martensite fraction that controls strength and crash energy absorption in automotive components [50]. Atomic size mismatch Δr quantifies lattice distortion and solid solution strengthening, both of which affect yield strength and impact toughness of structural steels [51]. The configurational mixing entropy ΔS_{mix} is a proxy for the chemical complexity that stabilises phases and delays transformation, which influences the stability of retained austenite and the balance of strength and ductility in advanced high-strength steels [52]. The carbon equivalent Ceq is a standard index for hardenability and weldability in structural practice; it correlates with the ease of forming martensite under cooling in thick sections and with heat-affected zone hardness and cold cracking risk in welded bridges and vehicle frames [53]. Prior austenite grain size and other microstructural variables were not included in the primary model because they are reported inconsistently across sources, depend strongly on processing history, and are not available for a large fraction of the dataset. Since the target variable is the M_s , which is primarily governed by chemical thermodynamics and the associated driving force, composition-based descriptors provide a robust and generalisable basis for prediction, while avoiding loss of coverage and potential information leakage from process-specific quantities.

Furthermore, empirical equations (M_s -Eq.1 to M_s -Eq.9) derived from previous studies were integrated into the model to leverage decades of metallurgical knowledge. These formulae encode well-established relationships between alloying elements and M_s , providing additional predictive power. By combining chemical, physical, and empirical inputs, the proposed model achieves improved accuracy and generalisability across a wide range of steel grades.

The calculation methods of the physical features are presented in Eqs. (1–4), and those of the empirical equation features are shown in Table 1. The target variable, M_s , represents the experimentally

Table 1

Summary of empirical equations (M_s -Eq.1 to M_s -Eq.9) for predicting M_s in steels.

No.	Equation	Ref.
1	$M_s = 539 - 423C - 30.39Mn - 12.14Cr - 17.69Ni - 7.46Mo$	[11]
2	$M_s = 531 - 391.2C - 43.3Mn - 21.8Ni - 16.2Cr$	[15]
3	$M_s = 499 - 292C - 32.4Mn - 22Cr - 16.2Ni - 10.8Si - 10.8Mo$	[20]
4	$M_s = 561 - 476C - 33Mn - 17Cr - 17Ni - 21Mo$	[16]
5	$M_s = 560.5 - 407.3C - 7.3Si - 37.8Mn - 20.5Cu - 19.5Ni - 19.8Cr - 4.5Mo$	[22]
6	$M_s = 521 - 353C - 22Si - 24.3Mn - 7.7Cu - 17.7Cr - 17.3Ni - 25.8Mo$	[12]
7	$M_s = 550 - 361C - 39Mn - 35V - 20Cr - 17Ni - 10Cu - 5Mo + 15Co - 30Al$	[14]
8	$M_s = 550 - 350C - 40Mn - 35V - 20Cr - 17Ni - 10Cu - 10Mo - 10W + 15Co$	[18]
9	$M_s = 538 - 317C - 33Mn - 28Cr - 17Ni - 11Si - 11Mo - 11W$	[21]

measured martensite start temperature. All features and the target were standardised to enhance training efficiency and numerical stability.

$$VEC = \sum C_i \bullet VEC_i \quad (1)$$

where C_i is the atomic fraction of the i -th element, and VEC_i is the valence electron count of the i -th element [48].

$$\Delta r = \sqrt{\sum C_i \bullet \left(1 - \frac{r_i}{\bar{r}}\right)^2} \quad (2)$$

where r_i is the atomic radius of the i -th element, and $\bar{r} = \sum C_i \bullet r_i$ is the average atomic radius [54].

$$\Delta S_{mix} = -R \bullet \sum C_i \bullet \ln(C_i) \quad (3)$$

where R is the gas constant (8.314 J/mol·K), and C_i is the atomic fraction of the i -th element [55].

$$Ceq = C + \frac{Mn}{6} + \frac{Cr + Mo + V}{5} + \frac{Ni + Cu}{15} \quad (4)$$

where C , Mn, Cr, Mo, V, Ni, and Cu are the weight percentages of the respective elements [56].

To accurately model the potential nonlinearities and interactions among these diverse features, a multi-branch Transformer fusion regression model was designed (as illustrated in Fig. 2). This model initially processes three categories of input features through separate MLP branches, each responsible for extracting high-level representations. These branches consist of several linear layers, ReLU activation functions, and dropout layers, and are tailored to handle the chemical composition inputs (15 dimensions), physical features (4 dimensions), and empirical equation features (9 dimensions), respectively. The extracted feature vectors from the three branches are then projected to a common dimension via linear transformations and subsequently fused using a Transformer encoder. This encoder incorporates multi-head self-attention mechanisms and feedforward neural networks, enabling effective modelling of global dependencies and complex interactions among features. The encoder output is subjected to mean pooling, followed by a fully connected regression layer that outputs the predicted M_s value.

Hyperparameters were optimised using Optuna. The selected configuration used for all reported results is given in Table 2, covering the branch widths, depths and dropout for each feature branch, the Transformer settings, and the main training parameters.

The Transformer is used only as a fusion module that operates on the three branch embeddings. The effective sequence length is therefore $L = 3$, so the self-attention complexity scales as $O(L^2)$ and is negligible in

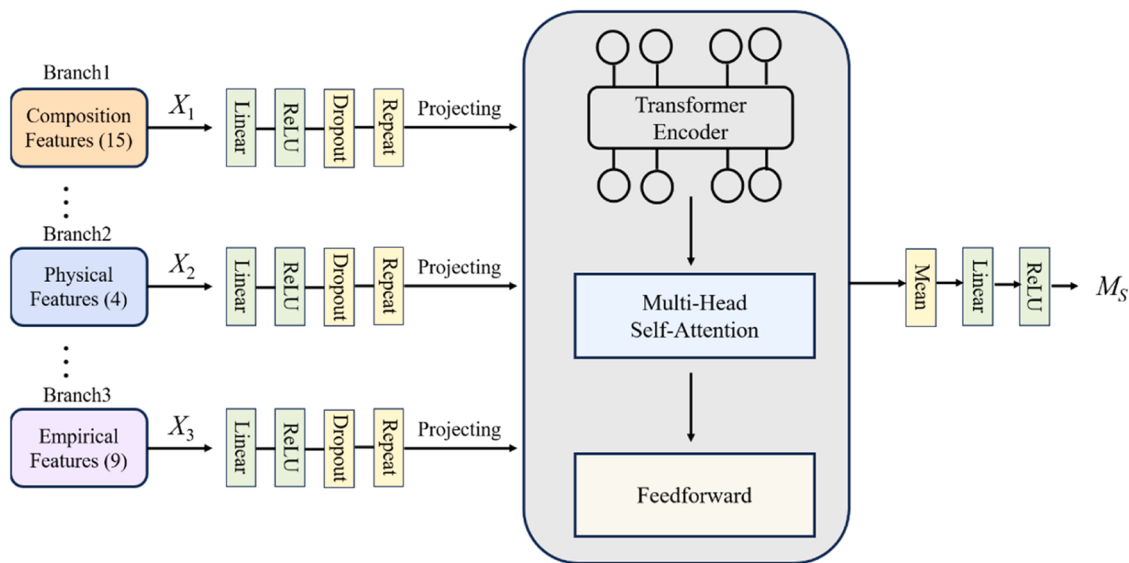


Fig. 2. Architecture of the multi-branch transformer fusion model for M_s prediction.

Table 2
Hyperparameters for the transformer fusion model.

Parameter	Branch 1 (Composition)	Branch 2 (Physical Features)	Branch 3 (Empirical Formulas)	Transformer Fusion
hidden units	128	80	112	
depth	2	1	1	
dropout	0.226	0.124	0.278	
learning rate (lr)				0.00071
batch_size				64
activation				ReLU
tf_d_model				128
tf_heads				4

both memory and time. This placement allows each branch to attend to the others and to capture higher-order cross-branch dependencies that are not well represented by simple concatenation, while keeping the computational footprint low. To control capacity and avoid overfitting, we use a single encoder block with a small hidden size together with dropout. Because the attention acts on a fixed and short fusion sequence rather than on the full set of 28 raw features, the approach remains efficient as the number of raw inputs grows, provided they are encoded within the same three branches. In ablation studies, we compare this fusion module with an additive attention fusion that replaces the encoder while keeping the branches unchanged, and with a graph neural network that treats the 28 features as nodes; the results reported in the revised manuscript support the choice of the Transformer fusion.

To comprehensively evaluate the performance of the proposed approach, five baseline models were established for comparative analysis: (1) an additive-attention fusion model that retains the three MLP branches and replaces the Transformer encoder with a single-head Bahdanau-style attention that produces a weighted sum of the branch embeddings; (2) a graph neural network model in which the 28 input features are treated as nodes in a fully connected graph and information is propagated by a two-layer graph attention network with global mean pooling; (3) an MLP model that integrates chemical composition, physical features, and empirical equations as concatenated inputs without branching; (4) an MLP model based solely on chemical composition features; and (5) a Lasso Regression model, which aims to discover explicit mathematical expressions that relate input features to M_s . All neural network models were optimised using the Optuna

framework for hyperparameter tuning under an identical search protocol, ensuring fairness and optimal performance, and were assessed through five-fold cross-validation to evaluate their robustness and generalisation capability. The optimal hyperparameters for each model are provided in the [Supplementary Material](#) under Hyperparameter Optimisation.

Evaluation metrics included mean squared error (MSE), mean absolute error (MAE), root mean squared error (RMSE), and the coefficient of determination (R^2), offering a comprehensive view of model performance in terms of both error magnitude and predictive correlation. The formulas for these metrics are as shown in Eqs. (5–7).

$$R^2 = 1 - \frac{\sum_{i=1}^n (y_i - \hat{y}_i)^2}{\sum_{i=1}^n (y_i - \bar{y})^2} \quad (5)$$

$$RMSE = \sqrt{\frac{1}{n} \sum_{i=1}^n (y_i - \hat{y}_i)^2} \quad (6)$$

$$PCC = \frac{n(\sum xy) - (\sum x)(\sum y)}{\sqrt{[n\sum x^2 - (\sum x)^2][n\sum y^2 - (\sum y)^2]}} \quad (7)$$

The methodological framework presented herein combines the nonlinear modelling capabilities of deep learning with the global feature interaction strengths of the Transformer architecture, offering a robust and generalisable approach for predicting M_s in complex material systems. The inclusion of baseline models serves to validate the effectiveness of the proposed method and provides theoretical and practical guidance for model selection in future applications such as material design and composition optimisation.

3. Results and discussion

3.1. Model training

To comprehensively evaluate the predictive performance of the proposed multi-branch Transformer fusion model, five representative models were selected for comparison, namely an additive-attention fusion model, a graph neural network model, an MLP-Combined model that concatenates all features without branching, an MLP-Chemical model that uses only chemical composition features, and a Lasso Regression model. The prediction results and performance metrics of each model are illustrated in Fig. 3.

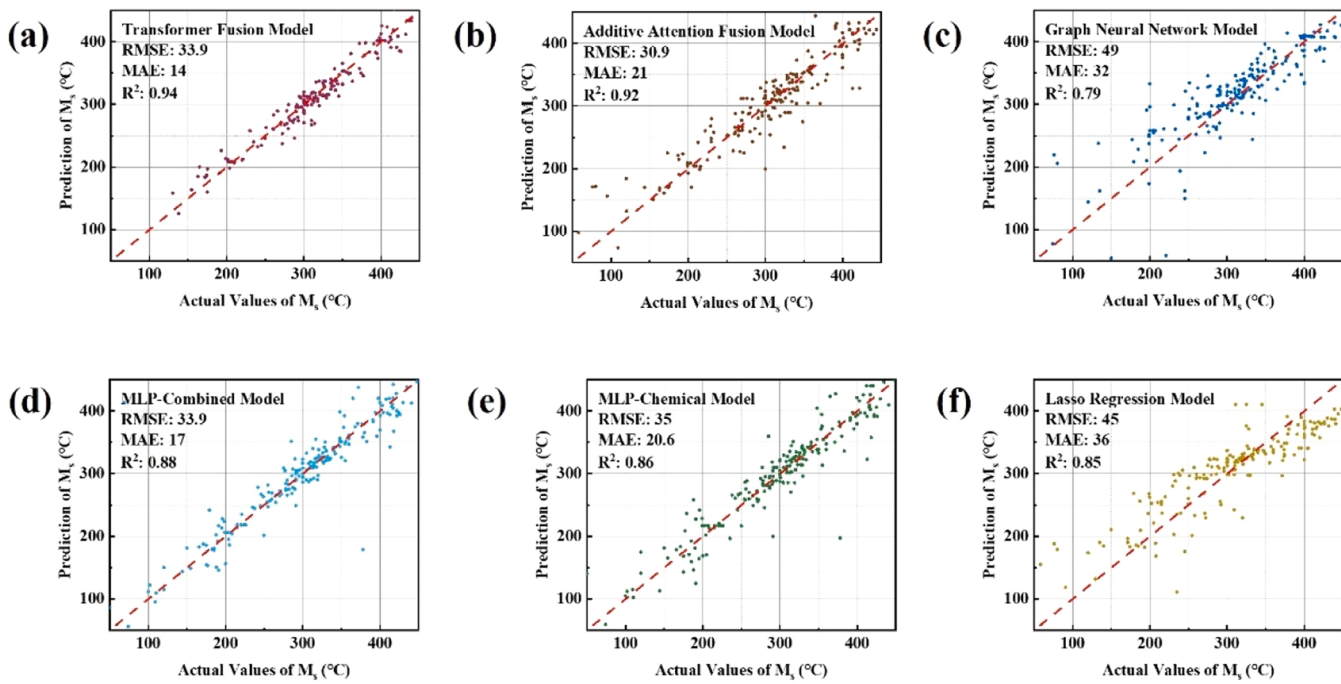


Fig. 3. Comparison of test-set M_s prediction across six models: (a) Transformer fusion, (b) additive attention fusion, (c) graph neural network, (d) MLP Combined, (e) MLP Chemical, and (f) Lasso regression; the Transformer shows the best overall accuracy ($R^2 = 0.94$, MAE = 14 °C, RMSE = 33.9 °C).

As shown in Fig. 3(a), the proposed Transformer fusion model achieved strong predictive performance on the test set, with an RMSE of 33.9 °C, MAE of 14 °C, and an R^2 of 0.94. These results indicate that the model effectively captures complex non-linear relationships and cross-branch interactions among the input features.

The additive-attention fusion model in Fig. 3(b) attained an RMSE of 30.9 °C, MAE of 21 °C, and R^2 of 0.92. Although the RMSE is slightly lower, the increased MAE and decreased R^2 suggest less consistent fidelity across samples relative to the Transformer fusion, indicating that multi-head self-attention provides added value for this task.

The graph neural network model in Fig. 3(c) yielded an RMSE of 49 °C, MAE of 32 °C, and R^2 of 0.79. Treating the 28 input features as nodes in a fully connected graph did not match the accuracy of the branch-level fusion, which may reflect the absence of a well-defined physical adjacency structure among features.

The MLP-Combined model in Fig. 3(d), which integrates chemical

composition, physical features, and empirical equation features without branching, achieved an RMSE of 33.9 °C, MAE of 17 °C, and R^2 of 0.88, indicating a marginally inferior fitting capability relative to the Transformer fusion.

The MLP-Chemical model in Fig. 3(e), which uses only chemical composition inputs, resulted in an RMSE of 35 °C, MAE of 20.6 °C, and R^2 of 0.86, highlighting the benefit of incorporating physical features and empirical equations.

The lasso regression model in Fig. 4(f) automatically derived mathematical expressions describing the relationship between M_s and the input features. The best-discovered equation is presented as Eq. (8). While lasso regression offers transparent and interpretable physical relationships, its predictive accuracy lags behind the deep learning models, with an RMSE of 45 °C, MAE of 36 °C, and R^2 of 0.85. This suggests that symbolic regression is better suited for discovering concise physical laws but is limited in modelling complex feature interactions.

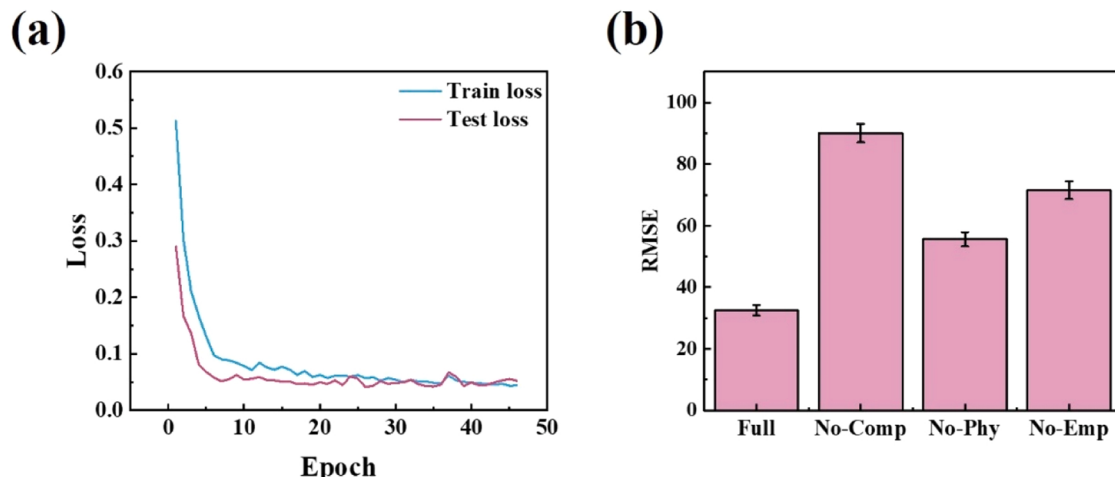


Fig. 4. (a) Training and testing loss curves for the Transformer fusion model, demonstrating stable convergence without overfitting. (b) Ablation study results for the Transformer fusion model, indicating the contribution of each feature group (composition, physical, empirical) to overall model performance in terms of RMSE.

$$\begin{aligned}
 M_s = & 419.5 - 195.5C - 0.27Cr - Co - 29.66C\cdot Mn \\
 & - 13.4C\cdot Ni - 2.99Mn\cdot Cr - 1.29Si^2 - 1.5Cr\cdot Ni - 0.5Ni^2 \\
 & + 7.25Mo\cdot Cu + 3.3Mo\cdot Nb + 53.5V\cdot Cu + 2592.5Al\cdot Cu + 90W\cdot Nb + \\
 & 11.2W\cdot Ti + 118.7Nb\cdot Ti
 \end{aligned} \quad (8)$$

Taken together, the results across all five comparators, namely the additive attention fusion model, the graph neural network model, the MLP-Combined model, the MLP-Chemical model, and the Lasso regression model, show that the multi-branch Transformer fusion offers the best overall balance of accuracy and robustness. It attains the highest R^2 (0.94) and the lowest MAE (14°C) while remaining competitive in RMSE, notwithstanding the slightly lower RMSE of the additive-attention baseline, which comes at the cost of reduced R^2 and increased MAE. These findings justify selecting the Transformer as the primary architecture for M_s prediction.

3.2. Model training dynamics and ablation study

To further validate the training performance of the proposed multi-branch fusion Transformer model and assess the significance of each feature branch, the training and validation loss curves were plotted, alongside an ablation study. The results are illustrated in Fig. 4.

Fig. 4(a) presents the training and validation loss trajectories of the Transformer model. It can be observed that both the training and validation losses decrease sharply during the initial epochs and subsequently stabilise, with no evident signs of overfitting. This indicates good convergence and generalisation capabilities of the model throughout the training process. The use of Optuna for hyperparameter optimisation proved effective in fine-tuning the model, ensuring robust performance.

To evaluate the contribution of each feature branch to the Transformer model, an ablation study was performed by removing in turn the chemical composition branch No-Comp, the physical features branch No-Phy, and the empirical equations branch No-Emp. The ablation was repeated over five independent 80–20 train to test splits, with retraining for every split and every condition. Fig. 4(b) reports the mean test RMSE, and the error bars indicate the standard deviation over the five runs. The complete model Full achieved an RMSE of 33.9°C . Removing chemical composition increased the RMSE to 88.2°C , indicating its dominant role in M_s prediction. Excluding the empirical equations branch and the physical features branch resulted in RMSEs of 71.2°C and 55.3°C , respectively. These results confirm that multi-source feature fusion improves accuracy, with chemical composition providing the largest contribution and the other branches offering additional but smaller gains.

The combined analysis of the loss curves and ablation study verifies the effectiveness and stability of the multi-branch fusion Transformer model, showcasing its potential for performance prediction in complex material systems.

3.3. SHAP analysis for model interpretability

To gain deeper insights into the internal mechanism of the Transformer fusion model, SHAP (SHapley Additive exPlanations) analysis was conducted, as shown in Fig. 5. This beeswarm plot visualises the individual contributions of each feature to the predicted M_s values across the dataset. The red and blue colour gradients indicate high and low standardised feature values, respectively, allowing interpretation of both the magnitude and direction of each feature's effect. For clarity, we present a single SHAP beeswarm after ranking features by mean absolute SHAP. Features with very small contributions, including B, Ti, and Nb, are omitted from the main panel.

C exhibits the most substantial impact on M_s predictions. Higher C

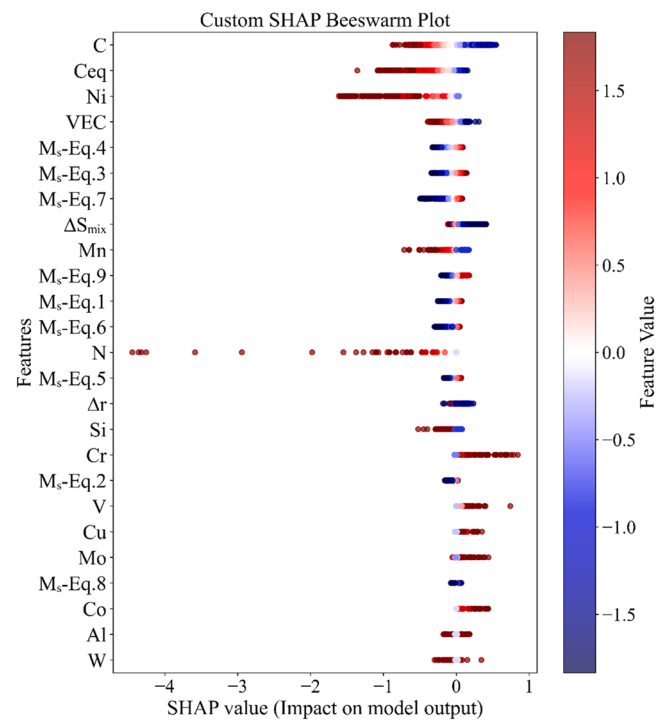


Fig. 5. SHAP beeswarm plot for the Transformer fusion model illustrating the contribution and directionality of each feature towards the predicted M_s , with red and blue indicating higher and lower standardised feature values, respectively.

content (shown in red) consistently shifts the predicted M_s towards lower values, reflecting its well-established role in lowering M_s due to increased hardenability. Ni contributes significantly as well, with lower Ni content (in blue) generally associated with higher M_s predictions. This aligns with Ni's function as an austenite stabiliser, which lowers M_s when present in higher amounts. Mn, another austenite stabiliser, demonstrates a behaviour similar to Ni; lower Mn levels (blue) elevate the predicted M_s , reflecting reduced austenite stability. N, though generally present in small amounts, shows a notable influence with higher N content (red) decreasing M_s , consistent with its strengthening and austenite-stabilising effects. Si shows a negative impact on M_s predictions, with higher Si content (red) associated with lower predicted M_s . This is likely due to Si's known effect of suppressing carbide formation, which leads to more carbon retained in austenite. The increased carbon stabilises austenite and lowers the M_s . Although Si also promotes ferrite formation, its effect on carbide suppression appears to dominate in this case. Cr exhibits a positive contribution to M_s predictions, with higher Cr content (red) generally associated with increased M_s . This may be related to its role in promoting ferrite formation and reducing austenite stability under certain conditions. In this dataset, the effect of Cr appears to favour a higher M_s when its content is elevated.

For the remaining alloying elements, such as V, Mo, Cu, Co, Al, and W, their SHAP distributions suggest more subtle contributions. In general, elements like Al and W tend to lower M_s when present in higher concentrations, while V, Mo, Cu, Co, Al, and W show minor positive effects, raising M_s slightly.

For the physical features, VEC and ΔS_{mix} both exhibit negative correlations with M_s . Higher VEC stabilises austenite through increased electron concentration, while greater mixing entropy promotes disordered structures, both leading to reduced M_s . Ceq shows a strong negative impact, highlighting the dominant role of carbon and substitutional alloying elements in suppressing martensitic transformation. Δr also displays a negative trend, where larger atomic size mismatches correlate with lower M_s , likely due to enhanced lattice distortion.

stabilising the austenitic phase.

To further quantify these findings, the next section will conduct a comprehensive element-wise sensitivity analysis, aiming to clarify the precise influence and relative strength of each key element on the M_s temperature. This analysis will help validate the SHAP interpretation results and support informed alloy design strategies.

Fig. 6 presents the chord diagram generated from SHAP interaction values, illustrating the collaborative interaction patterns among different features in the prediction of M_s . Each arc represents a specific feature, with the arc length indicating the proportion of its contribution to the total feature interactions. The connecting chords between arcs reflect the interaction strength between two features. In this diagram, colours are applied solely to distinguish between individual features for visual clarity, without encoding feature categories.

To enhance interpretability, empirical equation features (M_s -Eq.1 to M_s -Eq.9) are excluded from this diagram, as these equations are derived from chemical compositions and exhibit inherently strong interactions with elemental features, which would otherwise clutter the visualisation. Additionally, features with negligible contributions have been omitted to maintain diagrammatic simplicity and clarity. For the avoidance of doubt, these empirical quantities are outputs of composition-based martensite start equations and are algebraic transforms of the same elemental inputs. They are not application-specific indices, such as weldability measures and therefore their omission has no bearing on transportation-relevant interpretations. The interactions that matter for transportation steels, for example, those involving C, Ni and Ceq together with the physical descriptors, remain fully represented and the qualitative interaction pattern is unchanged.

The overall structure of the diagram is centred around the Ni-Ceq-C axis, with Ni serving as the dominant hub connected to multiple high-impact interactions. This central triad not only reflects their strong individual contributions to M_s prediction but also underscores their joint influence as revealed by the model's internal representation.

The strongest interaction is observed between Ni and Ceq. Although Ni is mathematically a component of Ceq [56], this interaction likely reflects more than formulaic overlap. The model appears to rely on both variables simultaneously, suggesting that Ni not only influences M_s directly but also modulates the interpretation of Ceq within the prediction process. This synergy may be due to Ni's dominant variation in the dataset or its physical role in austenite stabilisation.

The second-strongest pair, Ni- Δr , may reflect the combined influence of solute atom size mismatch and Ni's effect on stacking fault energy or local strain fields [57]. While this interaction aligns with known mechanisms in deformation-induced transformations, the specific role

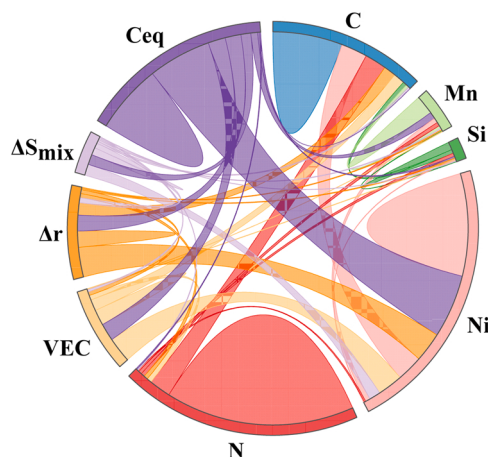


Fig. 6. Chord diagram illustrating the top 30 strongest feature interactions in the M_s prediction model, highlighting the dominant Ni-Ceq-C interaction network alongside key contributions from physical features such as Δr , ΔS_{mix} and VEC.

of Δr in the presence of Ni requires further study.

The Ni-C pair reflects a well-established synergy: Ni enhances carbon solubility and delays carbide formation, increasing the stability of austenite and suppressing martensitic transformation. This interaction has been extensively reported in both bainitic and martensitic steels [58].

The Ni-VEC interaction suggests a connection between alloying-driven changes in electron concentration and phase stability. VEC is known to influence phase formation, particularly in complex steels and high-entropy alloys [48], but its joint effect with Ni on M_s remains to be clarified through electronic structure studies.

The C-N interaction is consistent with the behaviour of interstitial elements: both carbon and nitrogen stabilise austenite, though through different mechanisms: C via thermodynamics and N through local lattice strain [59,60]. Their combined effect may create non-additive influences on transformation temperatures.

The interactions VEC-Ceq, Δr -Ceq, and C- Δr suggest that Ceq's predictive power may be modulated by underlying physical factors such as electronic density and lattice distortion. However, these patterns are data-driven discoveries rather than mechanisms with established metallurgical interpretation, and should be viewed as hypotheses for further investigation.

Finally, interactions such as Ni- ΔS_{mix} and C-VEC appear repeatedly in the model despite the absence of clear literature linking them directly to M_s . Their consistent contribution may reflect higher-order correlations or latent feature dependencies learned by the model, and thus merit additional theoretical or experimental exploration.

Overall, the chord diagram highlights that M_s prediction relies not only on individual feature strengths but also on learned interdependencies between them, some of which correspond well to established physical theory, while others represent novel insights potentially guiding future work.

3.4. Sensitivity analysis of individual elements

This set of sensitivity analysis plots, as shown in **Fig. 7**, illustrates the influence trends of various elemental concentrations on M_s across different compositional ranges. It further validates the model's ability to learn the intricate relationships between features and performance, while also cross-referencing with established metallurgical mechanisms from the literature to ensure scientific robustness. The following discussion elaborates on these effects in detail, structured according to elemental categories and supported by relevant studies.

Firstly, C exhibits a pronounced negative influence on M_s . As its content increases from 0 to approximately 2 wt%, M_s significantly decreases. This trend correlates strongly with carbon's high solubility in austenite. C stabilises the austenitic phase by occupying interstitial lattice sites, thereby suppressing the transformation to martensite [59]. Moreover, carbon increases the free energy difference between phases, further lowering M_s [61].

Both Mn and Si demonstrate negative effects, albeit with lesser magnitudes compared to carbon. Mn, up to 10 wt%, consistently reduces M_s by stabilising austenite. This is achieved through lowering the austenite-to-ferrite transformation temperature and increasing carbon solubility and stacking fault energy, which together suppress martensitic transformation [62]. Si (up to ~3 wt%) shows a similar trend, which is largely attributable to its indirect influence on carbon diffusion. As Si diffuses slowly within austenite, it inhibits carbide precipitation, thereby elevating carbon content within austenite and suppressing M_s [63]. Despite Si's inherent ferrite-stabilising effect thermodynamically, its interaction with carbon diffusion leads to an overall reduction in M_s .

Cr, within the range of 0–15 wt%, demonstrates a positive effect on M_s , with values rising as Cr content increases. This is attributed to Cr's role as a ferrite-stabilising element, which impedes the formation of austenite, thereby facilitating the martensitic transformation [56]. Cr also contributes through carbide formation, depleting carbon from the

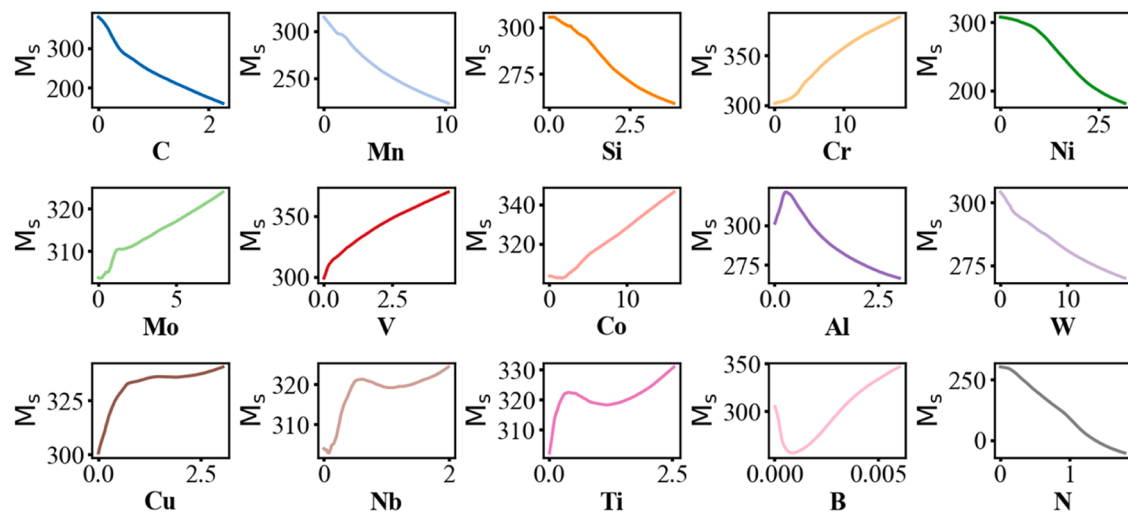


Fig. 7. Sensitivity analysis showing how variations in individual alloying element concentrations (wt%) influence the predicted M_s .

austenitic matrix and further promoting martensite formation [64].

The influence of Ni is particularly pronounced. As Ni content increases from 0 to 25 wt%, M_s decreases sharply by nearly 100°C. Ni is a potent austenite stabiliser, significantly lowering the free energy of austenite and broadening the austenitic phase field, which suppresses martensitic transformation [65]. This mechanism underpins the widespread application of Ni in austenitic stainless steels.

Mo and V exhibit positive influences on M_s , with Mo steadily increasing M_s up to ~6 wt% and V showing a notable rise in M_s within the 0–0.5 wt% range. Mo contributes through the formation of carbides (such as Mo₂C), which deplete carbon in austenite and destabilise it, enhancing martensite formation [66]. Mo also improves hardenability and optimises transformation pathways [67]. V facilitates similar effects via VC carbide precipitation, promoting grain refinement and reducing austenite stability, thereby elevating M_s [68].

Co increases M_s within the 0–10 wt% range, consistent with its role in destabilising austenite and enhancing ferrite stability. Co reduces the stability of the austenitic phase and narrows its compositional range, thereby promoting martensitic transformation, which is beneficial in high-strength steels and superalloys [69].

Al and W both enhance M_s . Al, particularly effective up to ~3 wt%, promotes M_s by stabilising ferrite and increasing the free energy difference between phases, which accelerates martensite formation [70]. W exhibits a more moderate effect within the 0–12 wt% range, primarily due to its carbide-forming ability (e.g., WC), which depletes carbon from the matrix and gradually destabilises austenite [71].

The effects of Cu and Nb are relatively modest but positive. Cu contributes by refining grains and enhancing precipitation hardening, which marginally increases M_s [72]. Nb, through the formation of NbC carbides, reduces carbon content in austenite and improves high-temperature strength and toughness, thereby slightly elevating M_s [73].

Ti and B, despite their low concentrations, exhibit appreciable effects on M_s . Ti promotes M_s through carbide precipitation (e.g., TiC), which removes carbon from austenite and destabilises it [74]. B, even in trace amounts, alters grain boundary characteristics and significantly modifies transformation kinetics, facilitating martensitic transformation [75].

Finally, N displays a marked negative influence on M_s . As N content increases (up to ~1.8 wt%), M_s decreases substantially. Like C, N stabilises austenite by dissolving interstitially within its lattice, significantly reducing its free energy and suppressing martensitic transformation [60]. Additionally, N forms nitrides, further enhancing austenite stability [76].

These sensitivity analyses reveal the nuanced influence of elemental

variations on M_s also align closely with metallurgical theories and experimental observations. This further validates the Transformer fusion model's capacity to capture complex feature-performance relationships, providing a robust theoretical foundation for alloy design, performance optimisation, and heat treatment strategies.

3.5. Experimental validation via dilatometry and microstructural characterisation

To evaluate the predictive capability of the developed Transformer-based model for the M_s , two designed steel alloys with distinct chemical compositions were experimentally investigated. The chemical compositions of the two steels are provided in Table 3. Alloy A was designed as a high-Si, medium-Ni martenitic composition with a comparatively higher M_s . The combination of Si and Al improves tempering resistance and oxidation resistance, while Mo supports strength at elevated temperature. This chemistry is representative of high-strength components that experience thermal cycling and dynamic loading in transport systems, for example energy-absorbing parts and spring-type hardware in under-bonnet environments. Alloy B was designed as a Ni- and Co-rich martenitic composition with a lower M_s . The higher Ni and Co depress M_s and improve toughness after tempering, and Al promotes precipitation hardening with Ni during tempering, providing hot strength and stability. This design motif is relevant to powertrain and exhaust-adjacent components and to thermally loaded fasteners in transportation applications. Together the two alloys span contrasting transformation windows and provide a practical validation of the model under heat-resistant design conditions pertinent to transportation use.

Dilatometry tests were conducted using a DIL 805 A/D dilatometer on cylindrical specimens (4 mm diameter × 10 mm length) machined from the hot-rolled plate. Each specimen was austenitised at 1000 °C for 30 min to ensure complete transformation to austenite, then cooled to room temperature under argon at a constant rate of 5 °C/s. The resulting dilatation-temperature curves were analysed to determine the experimental M_s , defined as the temperature at which a deviation from linear thermal contraction occurs.

Microstructural characterisation was carried out using a Leica

Table 3
Chemical compositions of the experimental alloys used for model validation (wt %).

Alloy	C	Si	Ni	Al	Mo	Mn	Co	Cr
A	0.72	3.87	3.4	1.39	0.21	0.02	<0.01	<0.01
B	0.45	0.03	13.2	2.63	0.15	0.15	3.99	<.005

Microsystems DM2500M upright optical microscope equipped with a DFC295 digital camera. Images were acquired using Leica Application Suite software, and minor post-processing (e.g., brightness/contrast adjustment, cropping, and scale bar insertion) was performed using GIMP and ImageJ.

For Alloy A, the martensitic transformation began at approximately 238 °C (Fig. 8(a)), while Alloy B exhibited an M_s of 169 °C (Fig. 8(c)). Optical microscopy was used to characterise the final microstructures. As shown in Fig. 8(b) and (d), both alloys displayed a typical lath martensite morphology after quenching. Notably, Alloy B showed a finer and denser structure, consistent with its lower transformation temperature.

To further validate generalisability, the two newly designed alloys were assessed. Fig. 9 compares the experimental M_s values with the predictions of the three models. The Transformer fusion model predicted 231 °C for Alloy A and 165 °C for Alloy B, in close agreement with the measured values of 238 °C and 169 °C, yielding absolute deviations of 7 °C and 4 °C. The additive attention fusion model produced 224 °C and 178 °C for Alloy A and Alloy B, corresponding to deviations of 14 °C and 9 °C. The MLP Combined model produced 255 °C and 158 °C, with deviations of 17 °C and 11 °C. These comparisons indicate that, for the available validation alloys, the Transformer fusion model provides the most accurate predictions.

4. Conclusion

This study proposed a novel multi-branch Transformer fusion model to predict the M_s in steels by integrating chemical composition, physical features, and empirical formula-based features. The model architecture, which combines individual MLP branches with Transformer-based attention mechanisms, effectively captures complex nonlinear

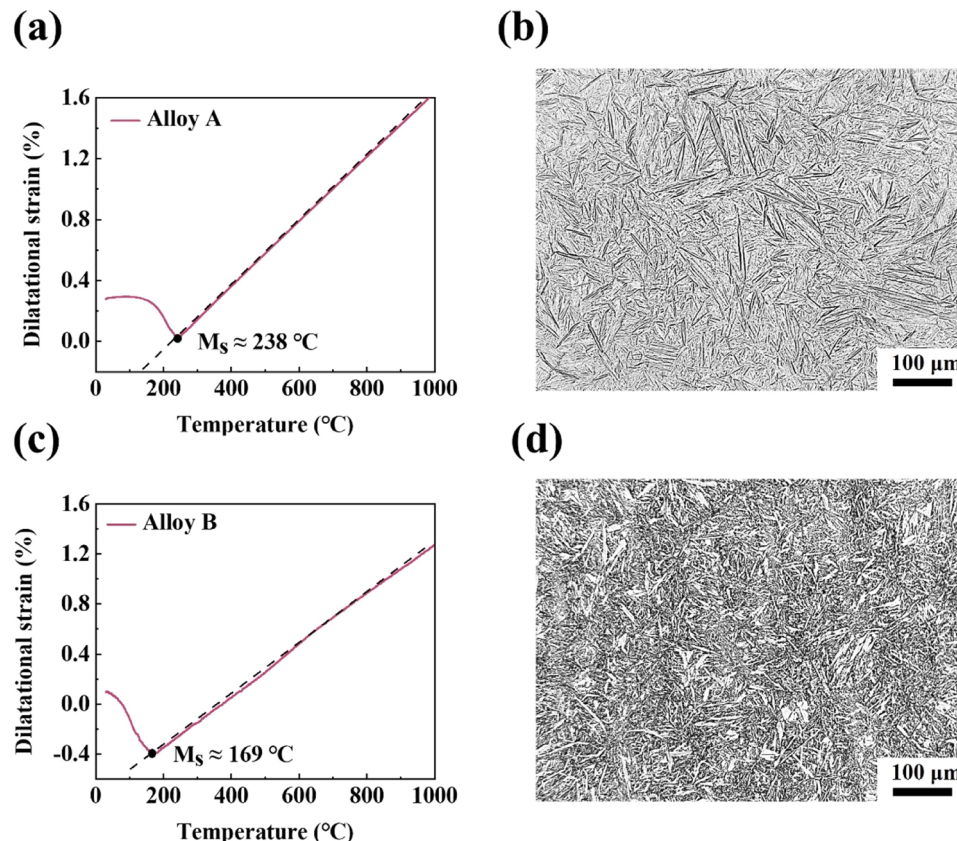


Fig. 8. Experimental Validation of predicted M_s values and corresponding microstructures for both alloys. (a) Dilatometry cooling curve for Alloy A showing $M_s \approx 238$ °C; (b) optical micrograph for Alloy A. (c) Dilatometry cooling curve for Alloy B showing $M_s \approx 169$ °C; (d) optical micrograph for Alloy B. Both alloys exhibit a fully martensitic microstructure after quenching.

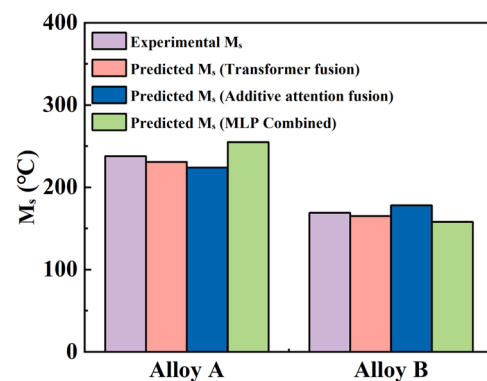


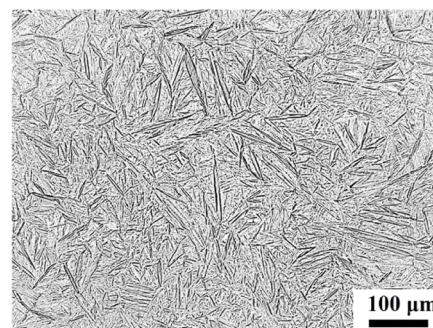
Fig. 9. Experimental and predicted M_s for Alloys A and B using Transformer fusion, additive attention fusion, and MLP Combined.

relationships and global feature interactions, achieving superior predictive performance ($RMSE = 33.9$ °C, $MAE = 14$ °C, $R^2 = 0.94$) compared to traditional MLP-based models and lasso regression approaches.

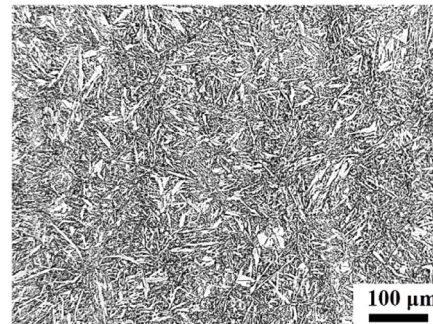
The ablation study demonstrated the essential contributions of each feature group, revealing that chemical composition serves as the primary determinant of M_s , while physical features and empirical equations significantly enhance predictive accuracy when incorporated within the Transformer fusion framework. This highlights the importance of multi-source feature integration in modelling complex metallurgical phenomena.

Furthermore, SHAP-based interpretability analysis provided critical insights into feature contributions and interactions, identifying C, Ni,

(b)



(d)



and Ceq as key influencing factors in M_s prediction. The chord diagram of feature interactions elucidated the dominant Ni–Ceq–C interaction network, as well as the moderating roles of physical features such as Δr and VEC, thereby validating the model's alignment with established metallurgical principles.

Element-wise sensitivity analysis further corroborated the model's ability to accurately capture the directional influence and relative strength of alloying elements on M_s , consistently reflecting classical metallurgical understanding. These results confirm that the proposed Transformer fusion model not only achieves high predictive accuracy but also offers mechanistic interpretability, bridging data-driven modelling with fundamental materials science.

Experimental validation on two designed steels confirmed the model's high predictive accuracy, with predicted M_s values (231 °C and 165 °C) showing excellent agreement with experimental measurements (238 °C and 169 °C), demonstrating its practical applicability and reliability for guiding alloy design.

Overall, this work demonstrates the potential of Transformer based architectures for advanced materials property prediction, providing a robust and interpretable framework for alloy design and optimisation. Future work may incorporate microstructural characteristics and thermo mechanical processing parameters to improve generalisation, and may address transportation applications by embedding service temperature histories and section thickness to represent cooling rate effects in infrastructure steels, by coupling the M_s predictor with process windows for press hardening and quenching and partitioning in vehicle components, and by including weldability descriptors such as carbon equivalent variants and surrogates for heat affected zone hardness and cracking susceptibility. External validation on bridge steels, rail grades, and press-hardened components will be undertaken to assess generalisation and practical utility.

CRediT authorship contribution statement

G.M.A.M. El-Fallah: Writing – review & editing, Visualization, Validation, Supervision, Methodology, Investigation, Formal analysis, Data curation, Conceptualization. **Pengxin Wang:** Writing – original draft, Visualization, Validation, Software, Methodology, Investigation, Data curation, Conceptualization.

Declaration of Competing Interest

The authors declare that they have no known competing financial interests or personal relationships that could have appeared to influence the work reported in this paper.

Acknowledgements

All authors gratefully acknowledge the support from Nanjing Iron & Steel United Co., Ltd. (NISCO), particularly for providing a PhD. scholarship for this study.

Appendix A. Supporting information

Supplementary data associated with this article can be found in the online version at [doi:10.1016/j.mtcomm.2025.113743](https://doi.org/10.1016/j.mtcomm.2025.113743).

Data availability

Data will be made available on request.

References

- [1] G.M.A.M. El-Fallah, H.K.D.H. Bhadeshia, Tensile behaviour of thermally-stable nanocrystalline bainitic-steels, Mater. Sci. Eng. A 746 (2019) 145–153, <https://doi.org/10.1016/j.msea.2018.12.124>.
- [2] G. Krauss, Martensite in steel: strength and structure, Mater. Sci. Eng. A 273–275 (1999) 40–57, [https://doi.org/10.1016/S0921-5093\(99\)00288-9](https://doi.org/10.1016/S0921-5093(99)00288-9).
- [3] M. Taylor, et al., The effect of compositional heterogeneity on the martensite start temperature of a high strength steel during rapid austenitisation and cooling, IOP Conf. Ser. Mater. Sci. Eng. 1249 (2022) 012061, <https://doi.org/10.1088/1757-899X/1249/1/012061>.
- [4] B. Xiao, et al., Uncovering the effect of retained austenite stability on the dynamic mechanical properties of TRIP-aided steel, Mater. Sci. Eng. A 942 (2025) 148729, <https://doi.org/10.1016/j.msea.2025.148729>.
- [5] B. Xiao, et al., Insights into the role of retained austenite stability in TRIP-aided steel: ductilizing and toughening, J. Mater. Res. Technol. 33 (2024) 7698–7708, <https://doi.org/10.1016/j.jmrt.2024.11.134>.
- [6] L. Wang, J.G. Speer, Quenching and partitioning steel heat treatment, Metall. Microstruct. Anal. 2 (2013) 268–281, <https://doi.org/10.1007/s13632-013-0082-8>.
- [7] Y. Fan, et al., Effect of microstructure on wear and rolling contact fatigue behaviors of bainitic/martensitic rail steels, Wear 508–509 (2022) 204474, <https://doi.org/10.1016/j.wear.2022.204474>.
- [8] G.M.A.M. El-Fallah, S.W. Ooi, H.K.D.H. Bhadeshia, Effect of nickel aluminide on the bainite transformation in a Fe-0.45C-13Ni-3Al-4Co steel, and associated properties, Mater. Sci. Eng. A 767 (2019) 138362, <https://doi.org/10.1016/j.msea.2019.138362>.
- [9] V.M. Salganik, et al., Analysis of structural and phase transformations in Low-Alloy steels based on dilatometric studies, Metallurgist 59 (2016) 766–773, <https://doi.org/10.1007/s11015-016-0172-3>.
- [10] G.M.A.M. El-Fallah, Dilatometric study of high silicon bainitic steels: solid-state transformations, Results Mater. 19 (2023) 100430, <https://doi.org/10.1016/j.rimma.2023.100430>.
- [11] K. Andrews, Empirical formulae for the calculation of some transformation temperatures, J. Iron Steel Inst. (1965) 721–727. (<https://cir.nii.ac.jp/crid/1573105975589242368>).
- [12] T. Kunitake, H. Ohtani, Calculating the continuous cooling transformation characteristics of steel from its chemical composition, Sumitomo Search 2 (1969) 18–21.
- [13] W. Steven, The temperature of martensite and bainite in low-alloy steels, J. Iron Steel Inst. 183 (1956) 349–359.
- [14] I. Tamura. Steel Material Study on the Strength, Nikkan Kogyo Shinbun Ltd, Tokyo, 1970, 40.
- [15] G. Eldis, Proceedings of the Symposium on the Hardenability Concepts with Applications to Steel, ed., Metallurgical Society of AIME, United States, 1977.
- [16] C. Kung, J. Rayment, An examination of the validity of existing empirical formulae for the calculation of ms temperature, Met. Trans. A 13 (1981) 328–331, <https://doi.org/10.1007/BF02643327>.
- [17] M. Peet, Prediction of martensite start temperature, Mater. Sci. Technol. 31 (2015) 1370–1375, <https://doi.org/10.1179/1743284714Y.0000000714>.
- [18] K. Monna, Tekko zairyō-gaku, Jikkō Shuppan Co. Ltd, 1972, p. 431.
- [19] S.M.C. van Bohemen, Bainite and martensite start temperature calculated with exponential carbon dependence, Mater. Sci. Technol. 28 (2012) 487–495, <https://doi.org/10.1179/1743284711Y.0000000097>.
- [20] R. Grange, The temperature range of martensite formation, Trans. Am. Inst. Min. Metall. Eng. 167 (1946) 467–501. (<https://cir.nii.ac.jp/crid/1573105975589247232>).
- [21] Y. Liu, Principle of Heat Treatment, China Mechanical Industry Press, Beijing, 1981.
- [22] T. Kunitake, Prediction of Ac1, Ac3 and ms temperature of steels by empirical formulas, J. Jpn. Soc. Heat. Treat. 41 (2001) 164–169. (<https://cir.nii.ac.jp/crid/1573668925150461440>).
- [23] C. Liu, H. Su, Prediction of martensite start temperature of steel combined with expert experience and machine learning, Sci. Technol. Adv. Mater. 25 (2024) 2354655, <https://doi.org/10.1080/14686996.2024.2354655>.
- [24] G. Ghosh, G.B. Olson, Computational thermodynamics and the kinetics of martensitic transformation, J. Phase Equilibria 22 (2001) 199–207, <https://doi.org/10.1361/105497101770338653>.
- [25] J.-W. Lee, et al., A machine-learning-based alloy design platform that enables both forward and inverse predictions for thermo-mechanically controlled processed (TMCP) steel alloys, Sci. Rep. 11 (2021) 11012, <https://doi.org/10.1038/s41598-021-90237-z>.
- [26] J. Chen, et al., Investigation on the interpretable machine-learning model for predicting mechanical properties of DH auto-steel plates, Mater. Today Commun. 46 (2025) 112674, <https://doi.org/10.1016/j.mtcomm.2025.112674>.
- [27] C. Capdevila, et al., Determination of ms temperature in steels: a Bayesian neural network model, ISIJ Int 42 (2002) 894–902, <https://doi.org/10.2355/isijinternational.42.894>.
- [28] J. Lu, et al., Classified dataset, regression and machine learning modeling for prediction of phase transformation temperatures in steels, Calphad 87 (2024) 102748, <https://doi.org/10.1016/j.calphad.2024.102748>.
- [29] S. Wang, et al., Predicting the martensite start temperature of steels via a combination of deep learning and multi-scale data mining, Comput. Mater. Sci. 246 (2025) 113430, <https://doi.org/10.1016/j.commatsci.2024.113430>.
- [30] Z. Yan, et al., New insight in predicting martensite start temperature in steels, J. Mater. Sci. 57 (2022) 11392–11410, <https://doi.org/10.1007/s10853-022-07329-y>.
- [31] M. Rahaman, et al., Machine learning to predict the martensite start temperature in steels, Metall. Mater. Trans. A 50 (2019) 2081–2091, <https://doi.org/10.1007/s11661-019-05170-8>.

- [32] X. Geng, et al., Modeling of CCT diagrams for tool steels using different machine learning techniques, *Comput. Mater. Sci.* 171 (2020) 109235, <https://doi.org/10.1016/j.commatsci.2019.109235>.
- [33] G. Ghosh, G. Olson, Kinetics of FCC→ BCC heterogeneous martensitic nucleation—I. the critical driving force for athermal nucleation, *Acta Metall. Mater.* 42 (1994) 3361–3370, [https://doi.org/10.1016/0956-7151\(94\)90468-5](https://doi.org/10.1016/0956-7151(94)90468-5).
- [34] K. Okazaki, T. Itoh, H. Conrad, The effect of grain size on the strength of a Ti-7.4 at %al alloy at low temperatures, *Trans. Jpn. Inst. Met.* 15 (1974) 159–166, <https://doi.org/10.2320/matertrans1960.15.159>.
- [35] D.L. Moffat, D.C. Larbalestier, The competition between the alpha and omega phases in aged Ti-Nb alloys, *Metall. Trans. A* 19 (1988) 1687–1694, <https://doi.org/10.1007/BF02645136>.
- [36] W.W. Cias, D.V. Doane, Phase transformation kinetics and hardenability of alloyed medium-carbon steels, *Metall. Trans.* 4 (1973) 2257–2266, <https://doi.org/10.1007/BF02669365>.
- [37] A. Sage, *Atlas of Continuous Cooling Transformation Diagrams for Vanadium Steels*, First Ed., Vanadium International Technical Committee, England, 1985.
- [38] A.Sf Metals, *Atlas of Isothermal Transformation and Cooling Transformation Diagrams*, Revised ed., American Society for Metals, Pittsburgh, PA, USA, 1977.
- [39] G. Ghosh, G.B. Olson, Kinetics of F.C.C. → B.C.C. heterogeneous martensitic nucleation—I. the critical driving force for athermal nucleation, *Acta Metall. Mater.* 42 (1994) 3361–3370, [https://doi.org/10.1016/0956-7151\(94\)90468-5](https://doi.org/10.1016/0956-7151(94)90468-5).
- [40] H.-j Xie, X.-c Wu, Y.-a Min, Influence of chemical composition on phase transformation temperature and thermal expansion coefficient of hot work die steel, *J. Iron Steel Res. Int.* 15 (2008) 56–61, [https://doi.org/10.1016/S1006-706X\(08\)60267-8](https://doi.org/10.1016/S1006-706X(08)60267-8).
- [41] S. Kaar, et al., New Ms-formula for exact microstructural prediction of modern 3rd generation AHSS chemistries, *Scr. Mater.* 200 (2021) 113923, <https://doi.org/10.1016/j.scriptamat.2021.113923>.
- [42] H.-S. Yang, H.K.D.H. Bhadeshia, Austenite grain size and the martensite-start temperature, *Scr. Mater.* 60 (2009) 493–495, <https://doi.org/10.1016/j.scriptamat.2008.11.043>.
- [43] C. Capdevila, F.G. Caballero, C. García De Andrés, Analysis of effect of alloying elements on martensite start temperature of steels, *Mater. Sci. Technol.* 19 (2003) 581–586, <https://doi.org/10.1179/026708303225001902>.
- [44] H.S. Yang, et al., Critical assessment: martensite-start temperature for the $\gamma \rightarrow \alpha'$ transformation, *Calphad* 36 (2012) 16–22, <https://doi.org/10.1016/j.calphad.2011.10.008>.
- [45] J. Zhang, et al., Effect of common alloying elements on α' martensite start temperature in titanium alloys, *J. Mater. Res. Technol.* 27 (2023) 4562–4572, <https://doi.org/10.1016/j.jmrt.2023.10.159>.
- [46] E. Hornbogen, The effect of variables on martensitic transformation temperatures, *Acta Met.* 33 (1985) 595–601, [https://doi.org/10.1016/0001-6160\(85\)90024-0](https://doi.org/10.1016/0001-6160(85)90024-0).
- [47] H. Bhadeshia, R. Honeycombe, Chapter 4 - solutes that substitute for iron, in: H. Bhadeshia, R. Honeycombe (Eds.), *Steels: Microstructure and Properties*, Fourth Edition, Butterworth-Heinemann, 2017, pp. 101–134.
- [48] S. Guo, et al., Effect of valence electron concentration on stability of fcc or bcc phase in high entropy alloys, *J. Appl. Phys.* 109 (2011), <https://doi.org/10.1063/1.3587228>.
- [49] Y. Zhang, et al., Microstructures and properties of high-entropy alloys, *Prog. Mater. Sci.* 61 (2014) 1–93, <https://doi.org/10.1016/j.pmatsci.2013.10.001>.
- [50] Y.-X. Guo, et al., Correlations between valence electron concentration and the phase stability, intrinsic strength, and deformation mechanism in fcc multicomponent alloys, *Phys. Rev. B* 109 (2024) 024102, <https://doi.org/10.1103/PhysRevB.109.024102>.
- [51] L. Li, et al., Lattice-distortion dependent yield strength in high entropy alloys, *Mater. Sci. Eng. A* 784 (2020) 139323, <https://doi.org/10.1016/j.msea.2020.139323>.
- [52] P.I. Odetola, et al., Exploring high entropy alloys: a review on thermodynamic design and computational modeling strategies for advanced materials applications, *Heliyon* 10 (2024) e39660, <https://doi.org/10.1016/j.heliyon.2024.e39660>.
- [53] Š. Talaq, The assessment of carbon equivalent formulas in predicting the properties of steel weld metals, *Mater. Des.* 31 (2010) 2649–2653, <https://doi.org/10.1016/j.matdes.2009.11.066>.
- [54] A. Takeuchi, A. Inoue, Calculations of mixing enthalpy and mismatch entropy for ternary amorphous alloys, *Mater. Trans. JIM* 41 (2000) 1372–1378, <https://doi.org/10.2320/matertrans1989.41.1372>.
- [55] R.A. Swalin, *Thermodynamics of solids* (Swalin, Richard A.), ed., ACS Publications, 1962.
- [56] G. Krauss, *Steels: Processing, Structure, and Performance*, second ed., ASM international, 2015.
- [57] R. Fussik, et al., Investigation of austenitic FeCrNi steels with regard to stacking-fault energy and thermal austenite stability, *Materialia* 3 (2018) 265–273, <https://doi.org/10.1016/j.mtla.2018.08.020>.
- [58] H.I. Aaronson, M. Enomoto, J.K. Lee, *Mechanisms of Diffusional Phase Transformations in Metals and Alloys*, CRC Press, 2016.
- [59] G. Krauss, Martensite in steel: strength and structure, *Mater. Sci. Eng. A* 273 (1999) 40–57, [https://doi.org/10.1016/S0921-5093\(99\)00288-9](https://doi.org/10.1016/S0921-5093(99)00288-9).
- [60] N. Krasokha, H. Berns, Study on nitrogen in martensitic stainless steels, *HTM J. Heat. Treat. Mater.* 66 (2011) 150–164, <https://doi.org/10.3139/105.110099>.
- [61] E. Sak-Saracino, H.M. Urbassek, Free energies of austenite and martensite Fe-C alloys: an atomistic study, *Philos. Mag.* 94 (2014) 933–945, <https://doi.org/10.1080/14786435.2013.870359>.
- [62] G. Grässel, et al., High strength Fe-Mn-(Al, Si) TRIP/TWIP steels development—properties—application, *Int. J. Plast.* 16 (2000) 1391–1409, [https://doi.org/10.1016/S0749-6419\(00\)00015-2](https://doi.org/10.1016/S0749-6419(00)00015-2).
- [63] B. Kim, J. Sietsma, M.J. Santofimia, The role of silicon in carbon partitioning processes in martensite/austenite microstructures, *Mater. Des.* 127 (2017) 336–345, <https://doi.org/10.1016/j.matdes.2017.04.080>.
- [64] I.A. Borisov, Effect of carbon, chromium, and nickel on carbide transformation in Cr-Ni-Mo-V-steels during tempering, *Met. Sci. Heat. Treat.* 32 (1990) 677–682, <https://doi.org/10.1007/BF00693336>.
- [65] N. Saenarjhan, J.-H. Kang, S.-J. Kim, Effects of carbon and nitrogen on austenite stability and tensile deformation behavior of 15Cr-15Mn-4Ni based austenitic stainless steels, *Mater. Sci. Eng. A* 742 (2019) 608–616, <https://doi.org/10.1016/j.msea.2018.11.048>.
- [66] P. Gong, et al., The effect of molybdenum on interphase precipitation and microstructures in microalloyed steels containing titanium and vanadium, *Acta Mater.* 161 (2018) 374–387, <https://doi.org/10.1016/j.actamat.2018.09.008>.
- [67] A. Gramlich, et al., Effect of molybdenum, aluminium and boron on the phase transformation in 4 wt.-% manganese steels, *Results Mater.* 8 (2020) 100147, <https://doi.org/10.1016/j.rinma.2020.100147>.
- [68] G. Yang, et al., Effects of vanadium on the microstructure and mechanical properties of a high strength low alloy martensite steel, *Mater. Des.* 50 (2013) 102–107, <https://doi.org/10.1016/j.matdes.2013.03.019>.
- [69] M. Maalekian, *The Effects of Alloying Elements on Steels (I)*. 2007, Graz University of Technology, Christian Doppler Laboratory for Early Stages of Precipitation: Graz (AUS).
- [70] G. Krauss, *Steels: heat treatment and processing principles*, first ed., ASM International, Materials Park, OH, 1989.
- [71] R.N. Hajra, et al., Influence of tungsten on transformation characteristics in P92 ferritic-martensitic steel, *J. Alloy. Compd.* 689 (2016) 829–836, <https://doi.org/10.1016/j.jallcom.2016.08.055>.
- [72] A.N. Bhagat, Study of the Phase Transformation Characteristics in Some Copper Bearing HSLA Steels. 2002, IIT Kharagpur.
- [73] S. Liu, et al., Significant influence of carbon and niobium on the precipitation behavior and microstructural evolution and their consequent impact on mechanical properties in microalloyed steels, *Mater. Sci. Eng. A* 683 (2017) 70–82, <https://doi.org/10.1016/j.msea.2016.11.102>.
- [74] Y. Han, et al., TiC precipitation induced effect on microstructure and mechanical properties in low carbon medium manganese steel, *Mater. Sci. Eng. A* 530 (2011) 643–651, <https://doi.org/10.1016/j.msea.2011.10.037>.
- [75] S. Koley, et al., Influence of boron on austenite to ferrite transformation behavior of low carbon steel under continuous cooling, *J. Mater. Eng. Perform.* 27 (2018) 3449–3459, <https://doi.org/10.1007/s11665-018-3459-7>.
- [76] X. Ma, et al., Effect of n on microstructure and mechanical properties of 16Cr5Ni1Mo martensitic stainless steel, *Mater. Des.* 34 (2012) 74–81, <https://doi.org/10.1016/j.matdes.2011.07.064>.